Dynamic modeling and experimental analysis of a novel bionic mantis shrimp robot

Dynamic modeling and experimental analysis of a novel bionic mantis shrimp robot

Gang Chen[1,2] | Yidong Xu[1] | Chenguang Yang[3] | Xin Yang[1] | Huosheng Hu[2] | Fei Dong[4] | Jingjing Zhang[5] | Jianwei Shi[5]

[1]School of Mechanical Engineering, Zhejiang Sci-Tech University, Hangzhou, China

[2]School of Computer Science and Electronic Engineering, University of Essex, Colchester, UK

[3]Department of Computer Science, University of Liverpool, Liverpool, UK

[4]Zhejiang Chengshi Robot Co., Ltd., Jiaxing, China

[5]Zhejiang CathayBot Technology Co., Ltd., Jinhua, China

Abstract

Small carnivorous marine animals have developed agile movement abilities through long-term natural selection, resulting in excellent maneuverability and high swimming efficiency, making them ideal models for underwater robots. To meet the requirements for exploring narrow underwater zones, this paper designs an underwater robot inspired by mantis shrimp. By analyzing the body structure and swimming mode of the mantis shrimp, we designed a robot structure and hardware system and established a dynamic model for the cou-pled motion of multiple pleopods. A series of underwater experiments were conducted to verify the dynamic model and assess the performance of the prototype. The experimental results confirmed the accuracy of the dynamic model and demonstrated that the bionic mantis shrimp robot can perform multiangle turns and flexible velocity adjustments and exhibits good motion performance. This approach provides a novel solution for developing robots suitable for detecting complex underwater environments.

KEYWORDS

bionic robots, dynamic modeling, mantis shrimp, multipleopod coupled motion, underwater exploration, underwater robots

1 | INTRODUCTION

The ocean is rich in natural resources, yet due to the complexity of the underwater environment, these resources have not been fully recognized and exploited (Chen, Zhao, et al., 2024; Pendergast & Lundgren, 2009; Reddy et al., 2021). Detecting narrow underwater environments poses significant challenges in ocean exploration (Cong et al., 2021; Ni et al., 2023). These environments, including rock crevices and underwater caves, often limit the movement and operation of detection devices (Am Ende, 2001; Weidner et al., 2017). The flexibility of robots is crucial for successful exploration in complex underwater environments (Chen, Xu, Wang, et al., 2024; Crespi et al., 2008). Inspired by natural creatures, underwater bionic robots offer advantages in terms of motion efficiency, maneuverability, and adaptability (Fu et al., 2021; Ren & Yu, 2021; Yu et al., 2018).

The mantis shrimp is a carnivorous arthropod that inhabits narrow underwater caves and coral reefs (Streets et al., 2022). It

FIGURE 1 Movement of mantis shrimp through coral. (a) Mantis shrimp encounters an obstacle. (b) Mantis shrimp deftly turns. (c) Mantis shrimp dives quickly. [Color figure can be viewed at wileyonlinelibrary.com]

possesses a flat body that is highly flexible, allowing for rapid swimming and agile maneuvering (Cheng et al., 2024). As shown in Figure 1, the mantis shrimp swiftly navigated through coral, showing its exceptional athletic prowess. In their recent study, Tadayon et al. explored the energy storage structure of the forelimb of mantis shrimp and elucidated its microstructure (Tadayon et al., 2015). Cox et al., on the other hand, developed Ninjabot, a robot that imitates the unique attack mechanism of the forelimb of mantis shrimp (Cox et al., 2014). Furthermore, Thoen et al. investigated the vision of the mantis shrimp and analyzed the underlying principles of its visual system (Thoen et al., 2014). While existing research has focused primarily on the working principles and visual structure of the forelimb of mantis shrimp, there is a conspicuous lack of research on overall motor structure and control (Ito et al., 2024; Xu et al., 2022).

The bionic mantis shrimp robot imitates the mantis shrimp using multiple pairs of pleopods and incorporates body bending to achieve flexible swimming. The interactions among these pleopods, body movements, and water are the primary factors responsible for propulsion and resistance (Chen et al., 2023). This dynamic process directly influences the swimming performance of the bionic mantis shrimp robot, providing a foundation for the development of flexible motion control in robotic systems. Consequently, it is crucial to focus on the dynamics of the swimming process of bionic mantis shrimp robots. Numerous studies have investigated the dynamics of various robots. For instance, Yang et al. explored the turning mobility of a bionic dolphin robot and developed a dynamic model that accurately predicts its turning motion (Yang et al., 2022). Our research group has studied the hydrodynamic model of a beaver-like robot, specifically examining the hydrodynamic properties of its webbed foot and stroke characteristics under different flow rates (Chen et al., 2021). Huang et al. proposed a flipper propulsion theory based on their analysis of the kinematics of cormorant fins during swimming, shedding light on the mechanisms underlying efficient thrust generation (Huang et al., 2016). Furthermore, Li et al. designed a bionic wire-driven manipulator capable of displacement and velocity amplification (Li et al., 2011). Finally, Alexander et al. explored the traveling-wave linear gait of snake-like robots and applied it to trajectory planning (Chang and Vela, 2020).

Currently, there is limited research on the dynamic modeling of webbed swimming for underwater bionic robots (Kashem & Sufyan, 2017; Wang et al., 2023, 2024). Furthermore, the motion of the bionic mantis shrimp robot is achieved through a combination of torso bending and pleopod movement, which sets it apart from snake-like robots and bionic fish robots that rely on body movement (Cao et al., 2021; Scaradozzi et al., 2017; Zhang et al., 2011). The existing dynamic methods are not suitable for analyzing the swimming process of the mantis shrimp robot, which has a flexible spine and multiple pleopod couplings. Therefore, it is crucial to thoroughly study the swimming dynamics modeling method of mantis shrimp robots. This paper aims to investigate the kinematics and swimming dynamics model of a bionic mantis shrimp robot, providing theoretical support for achieving precise motion control of the robot. The main contributions of this paper are as follows:

1 This paper analyzes the motion mechanism of the mantis shrimp and describes the structural and control system design of a bionic mantis shrimp robot with a flexible spine and multiple pleopods. The robot employs a rigid-flexible coupling design, utilizing materials such as photosensitive resin and carbon fiber in combination with flexible materials such as silica gel. The elastic deformation of the flexible material when subjected to an external force effectively meets the motion requirements of the robot in this study. Additionally, the overall structure of the robot is slender and flexible, enabling it to rapidly adjust its forward direction and swimming velocity in water, thereby adapting to narrow underwater environments.
2 Building upon the structure of a bionic mantis shrimp robot, this paper establishes a kinematic model of a rope-driven flexible spine and a kinematic model of a pleopod. Based on the coupled motion of multiple pleopods and their respective forces, the swimming dynamics model of the robot is formulated, providing a more accurate foundation for attitude adjustment and motion control of the robot. The kinematic and swimming dynamics models of the mantis shrimp robot are experimentally verified.

The remaining sections of this paper are organized as follows: Section 2 introduces the movement characteristics of the biological mantis shrimp, as well as the structure and hardware of the bionic mantis shrimp robot. Section 3 describes the kinematic modeling of the bionic mantis shrimp robot, while Section 4 analyzes and models the dynamics of the bionic mantis shrimp robot. Section 5 tests the swimming performance of the bionic mantis shrimp robot and verifies the dynamic model. Finally, Section 6 presents a brief discussion and conclusion.

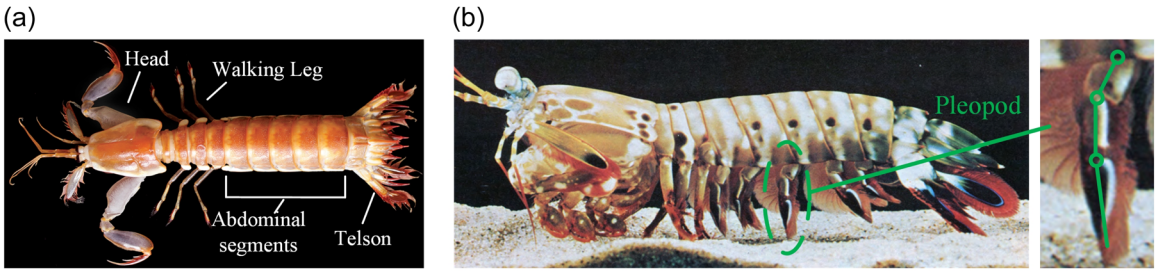

FIGURE 2 Mantis shrimp. (a) Top view. (b) Side view and enlarged view of the pleopod. [Color figure can be viewed at wileyonlinelibrary.com]

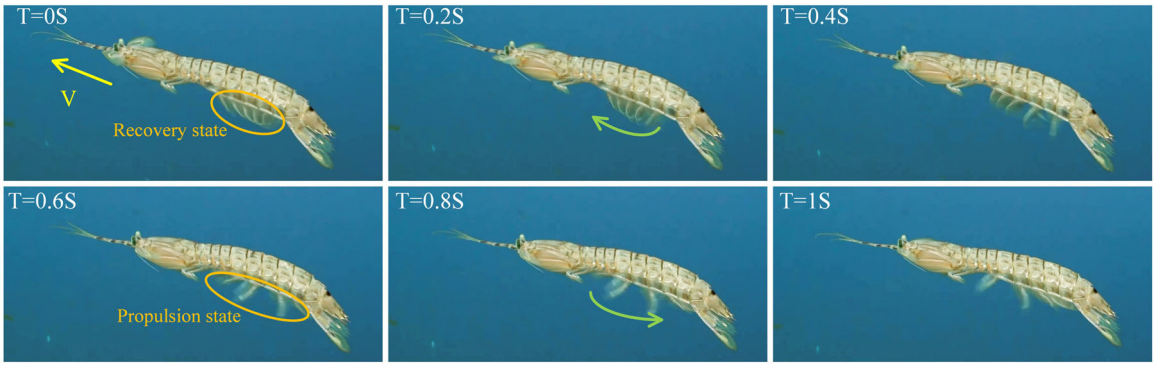

FIGURE 3 Biological mantis shrimp locomotion. [Color figure can be viewed at wileyonlinelibrary.com]

2 | DESIGN OF THE BIONIC MANTIS SHRIMP ROBOT

2.1 | Movement mechanism analysis of biological mantis shrimp

The mantis shrimp is a small predatory creature found in tropical and subtropical oceans. It inhabits narrow underwater caves and coral colonies, utilizing its flat and flexible body to freely maneuver (Chen, Xu, Yang, et al., 2024). As arthropods, the mantis shrimp relies on its pleopods to swim and is renowned for its remarkable speed in water (Patek, 2015). Figure 2 illustrates the main components of the mantis shrimp, including the head, abdominal segments, walking legs, swimming pleopods, and telsons. Its flat and agile body allows rapid swimming and agile turning through the coordinated movement of soft swimming pleopods. Additionally, the mantis shrimp can crawl underwater using its walking legs, further highlighting its proficiency in aquatic locomotion.

Pleopods play a fundamental role in the swimming abilities of mantis shrimp. Figure 3 depicts the motion states of the biological mantis shrimp within a 1-s interval. Notably, the swing angles of adjacent pleopods exhibit a consistent phase difference at any given moment. Furthermore, the pleopods function in two primary states during swimming: the propulsion state, wherein they are fully expanded to maximize forward propulsion, and the recovery state, wherein they are curved to minimize resistance.

2.2 | Structure and control system design of the bionic mantis shrimp robot

The design of the bionic mantis shrimp robot aims to replicate the natural shape and pleopod structure of the mantis shrimp, achieving comparable pleopod movements and exceptional swimming performance. Figure 4 presents our bionic mantis shrimp robot, which comprises the head, body, and telson. The head includes a waterproof box and controller, while the body consists of a flexible spine, rope, carbon fiber base, waterproof servo, pleopods, and pleopod base. The telson includes a telson base and bionic telson.

In the bionic mantis shrimp robot, the pleopods serve as the propulsion mechanism and are equipped with five pairs symmetrically distributed along the spine. Each pleopod is controlled by a waterproof servo, enabling individual adjustment of their movement status. The turning motion of the robot is facilitated by a wire rope driven by a servo. The dimensions of the bionic mantis shrimp robot designed in this study are approximately 750 mm in length and 150 mm in width, based on the physical dimensions of a reference biological mantis shrimp.

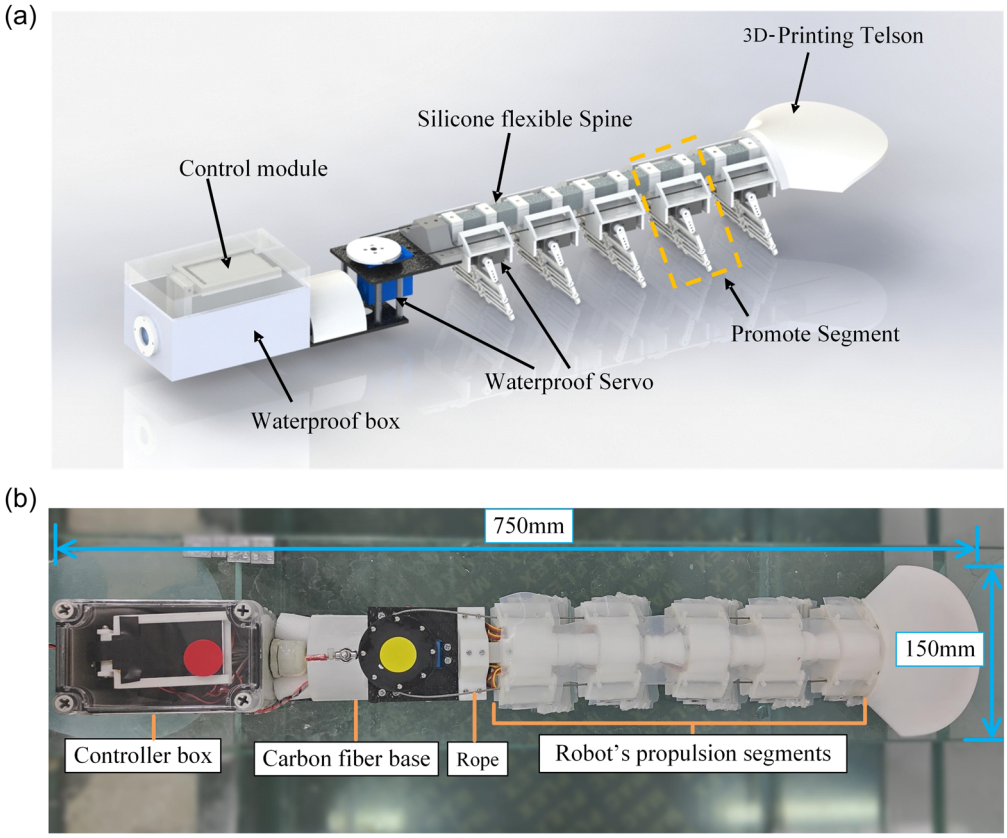

FIGURE 4 Design and prototype of the bionic mantis shrimp robot. (a) 3D rendering of the robot. (b) Physical drawing of robot. [Color figure can be viewed at wileyonlinelibrary.com]

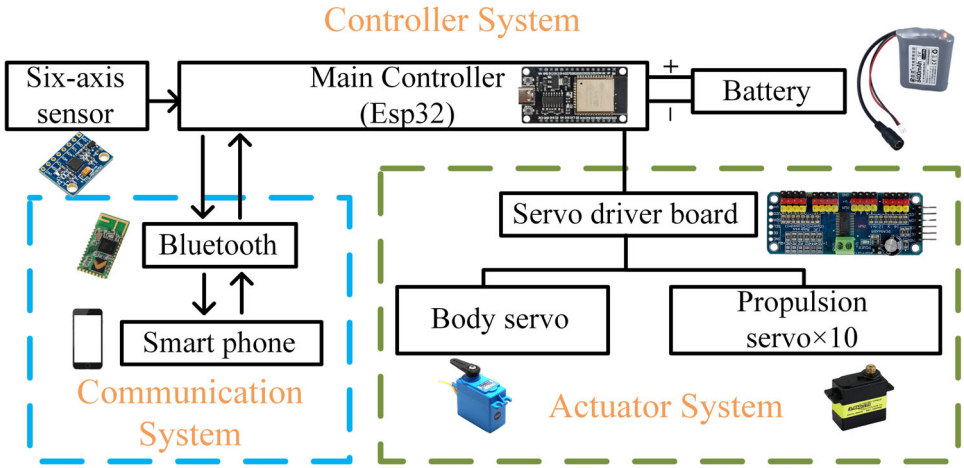

FIGURE 5 Block diagram of the bionic mantis shrimp robot control system. [Color figure can be viewed at wileyonlinelibrary.com]

The control system is utilized to coordinate the coupled motion between multiple pairs of pleopods and to implement motion control of our bionic mantis shrimp robot. It consists of five components: a controller, perceptron, joint actuator, communication module, and energy supply module. The robot can freely move using power from a battery, eliminating the need for an external power source. Figure 5 depicts the control system utilized for our bionic mantis shrimp robot, including a main controller (Espressif Systems ESP32) for controlling the sensor, actuators, and communication system; a servo driver board (Pulse-Width Modulation Controller 9685) for controlling the body servo (Hitec-5646 Waterproof Servo); 10 propulsion servos (Kingmax-0950 Mini Servo) for enabling swimming in water; a six-axis sensor (Inertial Measurement Unit 6050) for recording posture data; and a voltage management module (Xlsemi 4005). In the actuator system, the servo

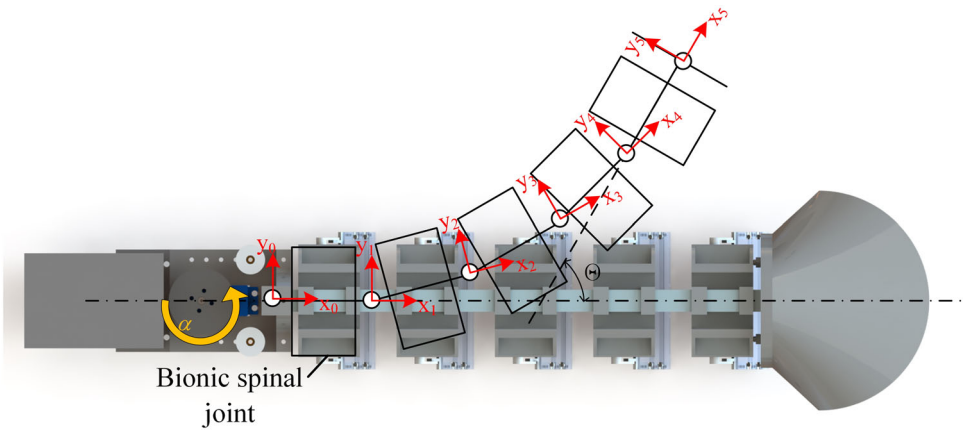

FIGURE 6 Robot body coordinate system definition. [Color figure can be viewed at wileyonlinelibrary.com]

driver board communicates with the main controller Esp32 through an Integrated Circuit and drives the servo to the desired angle based on the control signal sent from the main controller. The main controller, six-axis sensor, servo driver board, and voltage management module are integrated on a printed circuit board and placed in a waterproof box. The waterproof servos are positioned in corresponding parts of the body, with their power and signal lines connected to the servo driver board via a waterproof connector.

TABLE 1 D–H parameters of the robot body.

i	α_{i-1}	a_{i-1}	d_i	θ_i
1	0	P	0	0
2	0	P	0	θ_1
3	0	P	0	θ_2
4	0	P	0	θ_3
5	0	P	0	θ_4

3 | KINEMATIC MODELING OF THE BIONIC MANTIS SHRIMP ROBOT

3.1 | Kinematic modeling of the body

3.1.1 | Coordinate system definition of the body

Considering the structural design characteristics of the bionic mantis shrimp robot, its rope-driven flexible body is simplified into multiple virtual rigid links connected successively, and the center of rotation is located at the middle of two bionic spinal joints. The coordinate system for the robot body is established based on the D-H (Denavit-Hartenberg) method, as shown in Figure 6, where the rotation angle of the servo is denoted as α, and the counterclockwise direction is positive.

The gap between the assembly position of the first bionic spinal joint and the body base is small; therefore, its relative rotation is ignored and set as the reference coordinate system $x_0 o_0 y_0$ of the body coordinate system. The coordinate system $x_1 o_1 y_1$ to $x_4 o_4 y_4$ of the second to fifth joints is successively established. At this time, all joints are on a plane, and all are rotation joints. According to this coordinate system, the D-H parameters of the bionic flexible body can be obtained, as shown in Table 1, where i is the joint number, α_{i-1} is the link torsion angle, d_{i-1} is the link offset, and θ_{i-1} is the joint angle.

In Table 1, P is the length of the virtual link. According to the results of the structural design, the numerical size is the sum of the design width of the bionic spinal joint base and the gap. θ_i represents the rotation angle between the two biomimetic spinal joints, whose value is changed by the length of the wire rope pulled by the servo and satisfies $\theta_1 = \theta_2 = \theta_3 = \theta_4$.

3.1.2 | Kinematic modeling of the rope-driven flexible body

A servo is implemented to drive the rope-driven flexible body. This mechanism activates the wire rope attached to the steering wheel, resulting in a traction force at the other end of the wire rope. As shown in Figure 7, the joint kinematics of the rope-driven flexible torso include two levels of mapping. The parameter of the drive space is the change in rope length $\triangle l$. Its value is determined by the rotation angle of the servo, and its mathematical relation is expressed as follows:

$$\triangle L = \frac{\alpha \cdot r}{N}, \tag{1}$$

where r is the radius of the steering wheel and α is the rotation angle of the servo. The number of rotation joints on the body is assumed to be N.

The mapping between the drive space and the configuration space constitutes the first layer. This layer represents the kinematic mapping between the variation in rope length and the bending angle

of the robot's flexible body. The forward and inverse kinematics of this layer are defined as f_1 and f_1^{-1}, respectively. The mapping between the configuration space and task space is the second layer, which represents the kinematic relation between the bending angle of the robot's flexible body and the end coordinates (x, y) of the body. The forward and inverse kinematics are defined as f_2 and f_2^{-1}, respectively.

In terms of the second layer mapping, two connected bionic spinal joints can be represented as shown in Figure 8. When the flexible body remains unbent, the position relationship of the bionic spinal joint is demonstrated in Figure 8a. In this illustration, the black solid line corresponds to the wire rope, while the blue rectangle represents the bionic spinal joint. H_0 and D_0 are the height and width of the joint, respectively, and l_0 is the length of the wire rope between the two joints in this state. In this case, the lengths of the two wire ropes are equal. d_0 is the distance between the left and right sections of the wire rope when the wire rope passes through the reserved hole of the bionic spinal joint.

The position relationship of the bionic spinal joint when the flexible body is bent is shown in Figure 8a. The relation between the wire rope length and bending angle can be obtained:

$$\begin{cases} l_r = l_0 \cdot \cos\left(\frac{\theta}{2}\right) - d_0 \cdot \sin\left(\frac{\theta}{2}\right), \\ l_l = l_0 \cdot \cos\left(\frac{\theta}{2}\right) + d_0 \cdot \sin\left(\frac{\theta}{2}\right), \end{cases} \tag{2}$$

where l_l and l_r, respectively represent the lengths of the two wire ropes between the left and right joints in the bending state, θ is the angle between the adjacent bionic spinal joints, and the relationship between the maximum bending angle θ_{max} and the design parameters of the joint is as follows:

$$\theta_{max} = 2\arctan\left(\frac{l_0}{D_0}\right). \tag{3}$$

The mantis shrimp robot is equipped with five bionic spinal joints. The first joint, which is connected to the base of the head, has a small gap, and its bending angle can be considered negligible. Thus, the body has four rotatable joints.

When the relative angle of adjacent nodes is θ, the bending angle of the body is:

$$\Theta = N \cdot \theta. \tag{4}$$

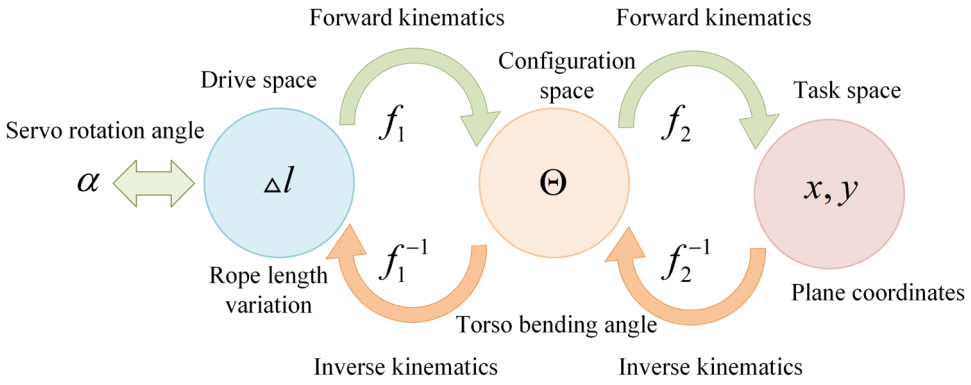

FIGURE 7 Kinematic mapping relation. [Color figure can be viewed at wileyonlinelibrary.com]

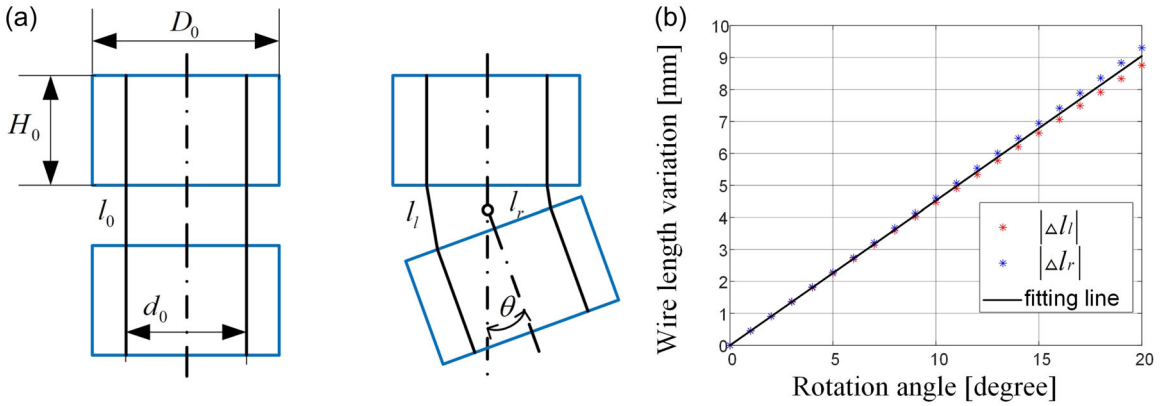

FIGURE 8 Schematic and numerical fitting results of the biomimetic spinal motion. (a) Initial and bending states of the bionic spine joint. (b) Numerical calculation and fitting results of bionic vertebral body rotation angle and wire rope length. [Color figure can be viewed at wileyonlinelibrary.com]

The length of the wire rope of the body is

$$\begin{cases} L_r = N \cdot (l_r + H_0), \\ L_l = N \cdot (l_l + H_0), \end{cases} \tag{5}$$

where L_0 is the wire rope length on one side of the rotation joint part of the flexible body in the initial state. In the initial state, the following relation is satisfied:

$$L_0 = N \cdot (l_0 + H_0). \tag{6}$$

However, when the flexible body is driven by the wire rope, the other side of the wire rope becomes relaxed. Therefore, for the purpose of kinematic analysis, we consider only the tension side of the wire rope. In this case, we focus on Figure 8b as an example, where the variation in the wire rope length on the tension side is given by:

$$\triangle L = L_0 - L_r = N \cdot \left(2l_0 \cdot \sin^2\left(\frac{\theta}{4}\right) + d_0 \cdot \sin\left(\frac{\theta}{2}\right)\right). \tag{7}$$

Combining Equations (4) and (7), we obtain

$$\triangle L = N \cdot \left(2l_0 \cdot \sin^2\left(\frac{\Theta}{4N}\right) + d_0 \cdot \sin\left(\frac{\Theta}{2N}\right)\right). \tag{8}$$

This is the inverse kinematics f_1^{-1} that expresses the mapping from the drive space to the configuration space. This formula can be used to determine the wire rope length based on the desired bending angle of the robot body. However, finding an analytical solution using this formula is relatively complex. We assume that the wire used by the rope traction mechanism does not deform and that the relative servo does not slip while maintaining tension between the joints. We also assume that the relative rotation angle between a set of adjacent joints is small and can be approximated as $\sin\theta \approx \theta$. Based on the design parameters of the bionic joint, the coordinates of the key points for two adjacent joints are defined, and the results shown in Figure 8b can be obtained through calculations involving rotation matrices. In the figure, the horizontal coordinate represents θ, while the vertical coordinate is the $\triangle l_l$ and $\triangle l_r$ obtained by operation. The change trend of the two values is close to that of the primary function. The proportional function is used to fit the data, and based on the above formula, the following relationship can be obtained:

$$\begin{cases} \triangle l = k\theta, \\ \Theta = \frac{\alpha r}{k}. \end{cases} \tag{9}$$

According to the fitting results, the fitting parameter $k = 0.45$ in the formula can be determined, where the unit of the body angle is radian (rad) and the unit of the rope length variation is millimeter (mm). The forward and inverse kinematics from the configuration space to the task space are used to calculate the coordinates of the body end in the robot body coordinate system and determine the current body bending angle based on these coordinates. The forward and inverse kinematics can be determined using the D-H parameter method discussed in the previous section. According to the D-H parameter table, when i=1, the joint homogeneous transformation matrix ${}_1^0T$ is:

$${}_1^0T = \begin{bmatrix} 1 & 0 & 0 & P \\ 0 & 1 & 0 & 0 \\ 0 & 0 & 1 & 0 \\ 0 & 0 & 0 & 1 \end{bmatrix}. \tag{10}$$

When i is greater than 1, the joint homogeneous transformation matrix from the $i-1$ to i coordinate system is:

$${}_i^{i-1}T = \begin{bmatrix} c\theta & -s\theta & 0 & Pc\theta \\ s\theta & c\theta & 0 & Ps\theta \\ 0 & 0 & 1 & 0 \\ 0 & 0 & 0 & 1 \end{bmatrix}, \tag{11}$$

where $c\theta$ and $s\theta$ are short for $\cos\theta$ and $\sin\theta$, respectively. Therefore, the forward kinematics f_2 from the configuration space to the task space are

$${}_5^0T = {}_1^0T{}_2^1T{}_3^2T{}_4^3T{}_5^4T. \tag{12}$$

Based on this formula, the coordinates of the endpoints of the bionic tail in the coordinate system of the robot joint can be calculated based on the bending angle of the body.

3.2 | Kinematic modeling of the bionic pleopod

3.2.1 | Coordinate system definition of the pleopod

The coordinate system of the pleopod joints is established based on the D–H method, taking into account the structural characteristics of the bionic mantis shrimp robot pleopod. Figure 9 illustrates the arrangement of the coordinate system. The first joint of the pleopod is an active joint controlled by servo movement. The second and third

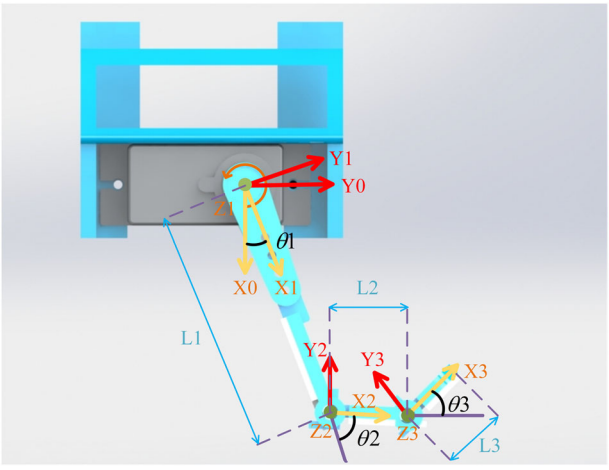

FIGURE 9 Bionic pleopod coordinate system definition.

TABLE 2 D–H parameters of the robot pleopod.

i	α_{i-1}	a_{i-1}	d_i	θ_i
1	0	0	0	θ_1
2	0	L1	0	θ_2
3	0	L2	0	θ_3

joints are passive and influenced primarily by mechanical limitations and water flow. The servo base is set as the reference coordinate system $x_0 z_0 y_0$, and the coordinate system $x_1 o_1 y_1$ to $x_3 o_3 y_3$ of the first to the third joints is established successively. Note that all joints are rotation joints on a Plane.

The D-H parameter table of the bionic pleopod can be established based on the coordinate system, as shown in Table 2. In this table, L1 and L2 represent the lengths of the joints, and θ_i represents the rotation angle between two joints whose value ranges from 0° to 90°.

3.2.2 | Kinematics of the pleopods

According to the D-H parameter table, when i= 1, the joint homogeneous transformation matrix ${}_1^0T$ is:

$$ {}_1^0T = \begin{bmatrix} c\theta_1 & -s\theta_1 & 0 & 0 \\ s\theta_1 & c\theta_1 & 0 & 0 \\ 0 & 0 & 1 & 0 \\ 0 & 0 & 0 & 1 \end{bmatrix}. \tag{13} $$

When is greater than 1, the joint homogeneous transformation matrix from the to coordinate system is

$$ {}_i^{i-1}T = \begin{bmatrix} c\theta_i & -s\theta_i & 0 & Li \\ s\theta_i & c\theta_i & 0 & 0 \\ 0 & 0 & 1 & 0 \\ 0 & 0 & 0 & 1 \end{bmatrix}, \tag{14} $$

where $c\theta$ and $s\theta$ are short for cos θ and sin θ, respectively. Therefore, the forward kinematics of the bionic pleopod are obtained:

$$ {}_3^0T = {}_1^0T {}_2^1T {}_3^2T. \tag{15} $$

Using this formula, the coordinates of each joint in the coordinate system of the pleopod can be calculated based on the motion angle of the servo. To achieve movement control of the five pairs of pleopods, we developed a central pattern generator controller for the bionic mantis shrimp robot. The mathematical model is as follows:

$$ \dot{\theta}_i = 2\pi v_i + \sum_j r_{1j} w_{ij} \sin(\theta_j - \theta_i - \varphi_{ij}), \tag{16} $$

$$ \ddot{r}_{1i} = \alpha_i \left(\frac{\alpha_i}{4} (R_{1i} - r_{1i}) - \dot{r}_{1i} \right), \tag{17} $$

$$ \ddot{r}_{2i} = \alpha_i \left(\frac{\alpha_i}{4} (R_{2i} - r_{2i}) - \dot{r}_{2i} \right), \tag{18} $$

$$ \ddot{x}_i = \alpha_i \left(\frac{\alpha_i}{4} (X_i - x_i) - \dot{x}_i \right), \tag{19} $$

$$ \beta_i = x_i + r_{1i} \cos\theta + r_{2i} \sin\theta, \tag{20} $$

where v_i is the desired frequency of the oscillator. ω is the angular frequency of the oscillator $\omega = 2\pi v_i$. x_i, r_{2i}, and r_{1i} are the amplitude state variables of the output deviation term, sine term, and cosine term in oscillator i, respectively. α_i refers to constant positive gains. w_{ij} and φ_{ij} are the coupling weights and phase biases, respectively, which determine how oscillator j influences oscillator i. R_{1i}, R_{2i}, and X_i are the parameters of the controller representing the desired amplitude of each corresponding output term of the oscillator. β_i represents the final output angle of each oscillator.

4 | SWIMMING DYNAMIC MODELING OF THE BIONIC MANTIS SHRIMP ROBOT

4.1 | Force analysis of the pleopods

The propulsion of the bionic pleopod essentially comes from the fluid resistance generated when the pleopod moves, and its force analysis is shown in Figure 10, where v is the motion velocity of the robot, β is the swing angle of the bionic pleopod, and ω_1 and ω_2 represent the swing angular velocities of the bionic pleopod in the propulsion and recovery states, respectively. Figure 10b illustrates the propulsion and recovery states of the pleopod, with each pleopod having a motion range of 90°. When the pleopod swings to the rear of the robot, its velocity is in the negative x-axis direction relative to the water flow, resulting in forward propulsion for the robot. Conversely, when the pleopod swings to the front of the robot, resistance is generated to impede the robot's progress.

Under the assumption that the water flow remains stationary without considering eddies and other complex conditions, the fluid resistance can be expressed as:

$$ f = \frac{1}{2} C_T \rho v^2 S, \tag{21} $$

where C_T is the fluid resistance coefficient, ρ is the fluid density, v is the relative fluid flow rate, that is, the moving velocity of the robot in standing water, and S is the frontal area.

By dividing the microelements along the y-axis on the bionic pleopod, the force generated by the bionic pleopod on the x-axis can be obtained as follows:

$$ T_x = \begin{cases} \frac{1}{2} C_T \rho \int_0^{l \sin\beta} (\omega_1 r_{(x)} - v)^2 W dy, & \text{Propulsion state,} \\ \frac{1}{2} C_T \rho \int_0^{l_0 \sin\beta} (\omega_2 r_{(x)} + v)^2 W dy, & \text{Recovery state,} \end{cases} \tag{22} $$

where W is the width of the bionic pleopod. l and l_0 are the maximum projection lengths of the pleopod in the propulsion and

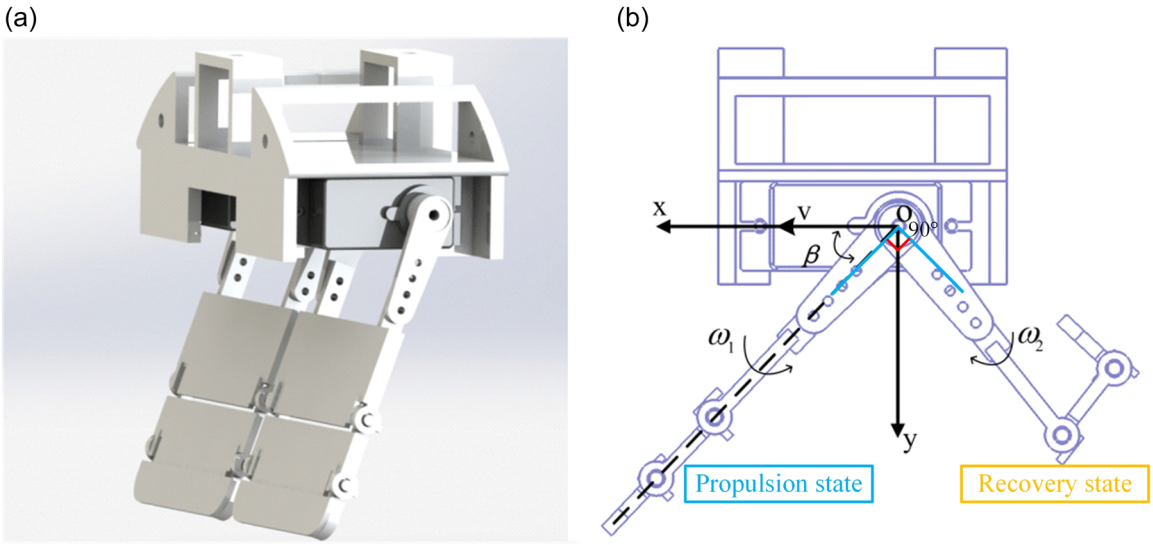

FIGURE 10 Force analysis diagram of bionic pleopods. (a) Bionic pleopod joints. (b) Two states of the bionic pleopod. [Color figure can be viewed at wileyonlinelibrary.com]

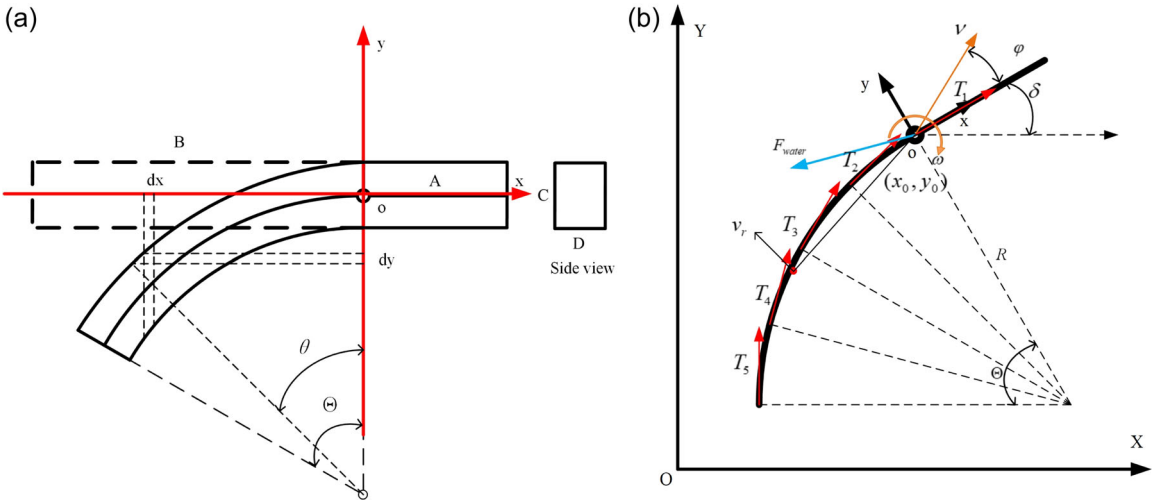

FIGURE 11 Robot coordinate system and its simplified model. (a) Robot coordinate system and its simplified model definition. (b) The definition of the body and its motion state in the world coordinate system. [Color figure can be viewed at wileyonlinelibrary.com]

recovered state on the y-axis, respectively. $\omega_1 r_{(x)}$ and $\omega_2 r_{(x)}$ are the projections of the linear velocity of a microelement of the pleopod on the *x*-axis.

4.2 | Dynamic modeling of the robot

The surface shape of the bionic mantis shrimp robot is complex, making comprehensive force analysis challenging. Consequently, a simplified model, as depicted in Figure 11a, can be derived by abstracting and simplifying its 3D model. The body coordinate system is established with the junction between the bendable body and the robot's head as the reference point. The positive *x*-axis points toward the robot's head. From a side view, the robot is simplified as a rectangle with a cross-sectional size of C × D. In the top view, the robot is divided into two sections. The positive part on the *x*-axis represents the fixed section of the robot's head, measuring A in length, while the negative part on the *x*-axis represents the bionic bendable body of the robot, measuring B in length. The dotted line shows the state of the robot without bending. When the bionic body bending angle is Θ, the bending state of the robot is shown as a solid line.

As illustrated in Figure 11b, the kinematic model of the bionic mantis shrimp robot was established, and the relationship between the robot and the world coordinate system was defined. This model is based on the following assumptions: the robot's motion does not experience sudden changes, and posture changes are not considered. Additionally, the robot's motion state at the next moment is solely influenced by the current motion speed and the bending angle of the flexible body.

In Figure 11b, *XOY* is the world coordinate system, and the bionic mantis shrimp

The robot is simplified and represented by the thick black line. The origin of the body coordinate system *xoy* in the world coordinate system coordinates is (x, y). The angle between the coordinate systems is δ. The rotation angular velocity and linear velocity are ω and v, respectively, in the body coordinate system, and the angle between the velocity direction and the x-axis is defined as φ.

In the bionic robot body, the bending angle of the body is Θ, and θ is the bending angle corresponding to a point on the torso. T_i is the force generated on the robot when the pleopod pair i swings, and its direction is the tangent direction of the body arc where the pleopod is located. F_{water} is the fluid resistance generated when the robot moves in the water, and M_{water} is the fluid resistance moment generated when the robot rotates in the water.

According to the geometric relationship shown in Figure 11b, the following relations can be obtained:

$$\begin{cases} x_{t+1} = x_t + v_t \cdot \cos(\varphi + \delta) \cdot dt, \\ y_{t+1} = y_t + v_t \cdot \sin(\varphi + \delta) \cdot dt, \\ \delta_{t+1} = \delta_t + \omega_t \cdot dt, \\ v_t = v_{t-1} + \vec{a} \cdot dt, \\ \omega_t = \omega_{t-1} + \alpha \cdot dt. \end{cases} \tag{23}$$

Then, the force balance equations along the *x*-, *y*-, and *z*-axes are established as follows:

$$\begin{cases} m\ddot{x} = F_x^{water} + F_x^{foot}, \\ m\ddot{y} = F_y^{water} + F_y^{foot}, \\ I_z\ddot{\beta} = M^{water} + M^{foot}, \end{cases} \tag{24}$$

where F_x^{water}, F_y^{water}, F_x^{foot}, and F_y^{foot} are the components of the fluid resistance to the robot and the propulsion generated by the bionic pleopod on the *x* and y-axes, respectively, and *m* represents the mass of the robot. M^{water} and M^{foot} are the resistance moment generated by the fluid on the robot and the propulsion moment generated by the bionic pleopod, respectively. The calculation formula is as follows:

$$F_x^{water} = \begin{cases} -\frac{1}{2}C_T\rho \cdot \left\{ (v\cos\varphi)^2 \cdot CD + \int_{R\cos\Theta-R}^{-\frac{1}{2}C} (\omega y + v\cos\varphi)^2 \right. \\ \qquad \left. dy \right\} \ \Theta \neq 0, \\ -\frac{1}{2}C_T\rho \cdot (v\cos\varphi)^2 \cdot CD \ \ \Theta = 0, \end{cases} \tag{25}$$

$$F_x^{foot} = \begin{cases} \sum_{i=0}^{4} T\cos\left(\frac{i\Theta}{4}\right) \ \Theta \neq 0, \\ 5T \ \ \Theta = 0, \end{cases} \tag{26}$$

$$F_y^{water} = \begin{cases} -\frac{1}{2}C_T\rho \cdot \int_{-R\sin\Theta}^{A} (\omega x + v\sin\varphi)^2 D dx \ \ \Theta \neq 0, \\ -\frac{1}{2}C_T\rho \cdot \int_{-B}^{A} (\omega x + v\sin\varphi)^2 D dx \ \ \Theta = 0, \end{cases} \tag{27}$$

$$F_y^{foot} = \begin{cases} \sum_{i=0}^{4} T\sin\left(\frac{i\Theta}{4}\right) \ \Theta \neq 0, \\ 0 \ \ \Theta = 0. \end{cases} \tag{28}$$

I_z is the moment of inertia of the robot about the *z*-axis, which can be calculated as follows:

$$I_z = \begin{cases} \int_{-R\sin\Theta}^{0} \frac{2x^2}{1+\sqrt{1-x^2}} \cdot CD\rho dx + \int_0^A CD\rho x^2 dx \ \ \Theta \neq 0, \\ \int_{-B}^{A} CD\rho x^2 dx \ \ \Theta = 0. \end{cases} \tag{29}$$

Accordingly, the expressions for M^{water} and M^{foot} are as follows:

$$M^{water} = \begin{cases} \int yd(F_x^{water}) + \int xd\left(F_y^{water}\right) \ \Theta \neq 0, \\ \frac{1}{2}C_T\rho D\int_{-B}^{A} (\omega x + v\sin\varphi)^2 x dx \ \ \Theta = 0, \end{cases} \tag{30}$$

$$M^{foot} = \begin{cases} \sum_{i=0}^{4} TR(1 - \cos\left(\frac{i\Theta}{4}\right) \ \Theta \neq 0, \\ 0 \ \ \Theta = 0. \end{cases} \tag{31}$$

5 | SWIMMING EXPERIMENTS OF THE BIONIC MANTIS SHRIMP ROBOT

To validate the accuracy of the swimming dynamics of the bionic mantis shrimp robot and further investigate its swimming performance, an experimental platform was constructed for robot swimming, as depicted in Figure 12. The dimensions of the experimental tank were 2 m × 1 m × 1 m (length × width × height). Figure 12a shows the robot swimming experimental platform equipped with an image acquisition capability. A camera is installed on top of the water tank to obtain the motion parameters of the robot by analyzing the graphic time series during the experiment. Figure 12b illustrates the robot swimming experimental platform equipped with a force sensing capability, which can measure the dynamic parameters of the robot swimming process using the ME K6 six-axis force sensor. The sampling frequency of the force sensor is 10 Hz, and the data is recorded every 0.1 s. The maximum control frequency of the central pattern generator controller is 1.5 Hz. The sampling frequency of 10 Hz has been able to record the movement of the pleopod, which has met our experimental goal.

5.1 | Straight swimming experiment

5.1.1 | Straight swimming velocity

The locomotion of mantis shrimp primarily involves the continuous swinging of their pleopods, as indicated by an analysis of their swimming morphology. To assess the linear swimming performance of the robot, we conducted tests to measure the average swimming velocity of the robot under different frequencies and phases.

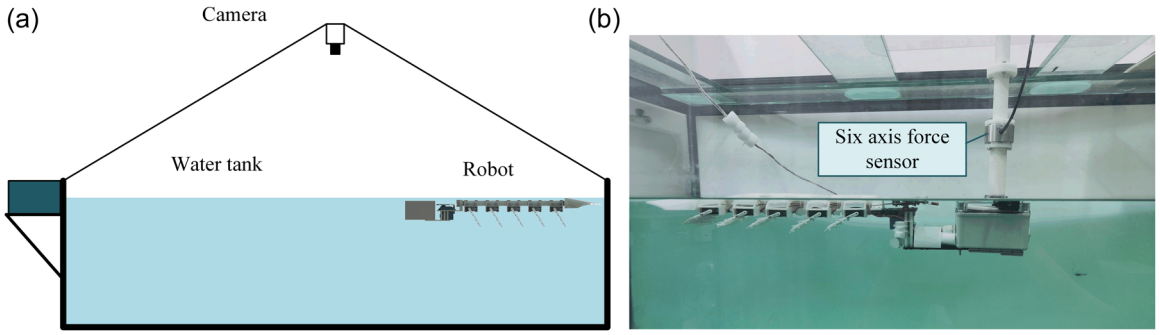

FIGURE 12 Swimming experimental platform of the bionic mantis shrimp robot: (a) image acquisition function and (b) force sensing function. [Color figure can be viewed at wileyonlinelibrary.com]

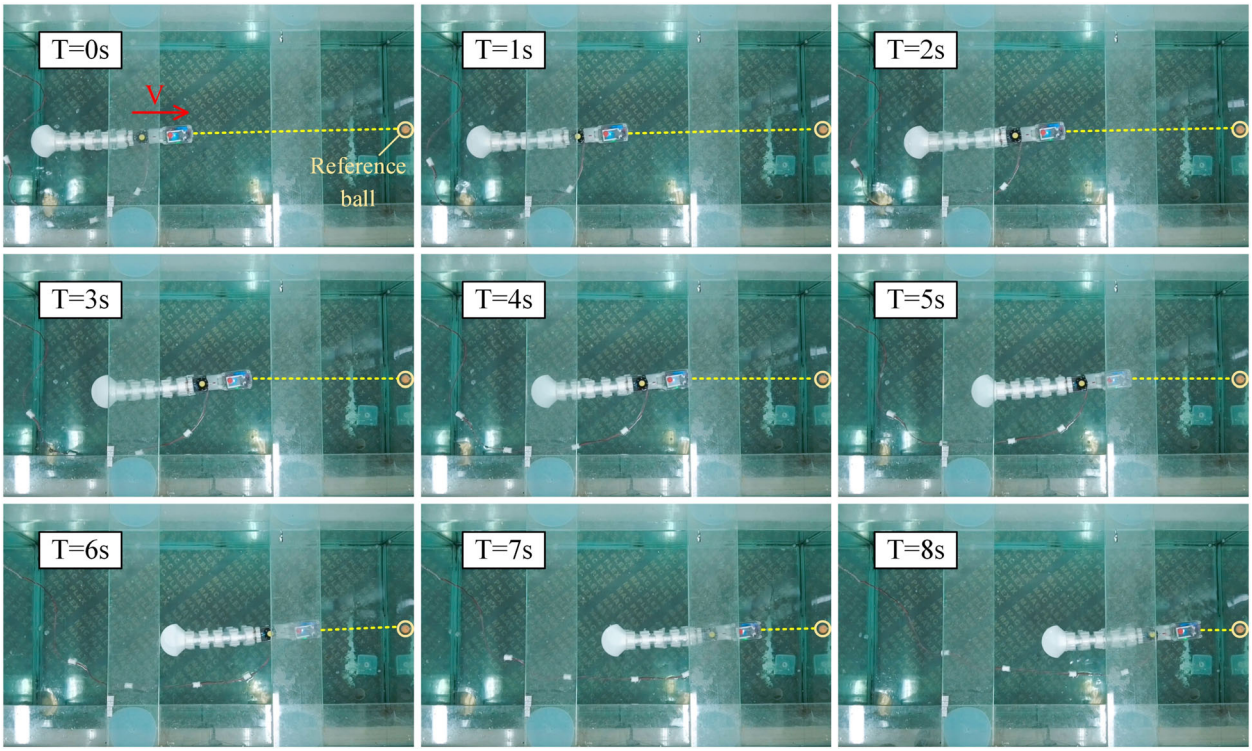

FIGURE 13 Sequence diagram of the straight motion process of the robot.

The angular frequency ranged between π and 2.5π (rad/s), while the phase difference ranged from 0 to $1/5Fre$, where $Fre = 3/4\pi$. *Fre* is a phase value determined through multiple experiments, ensuring that adjusting the phase difference does not interfere with the movement of multiple pleopods. A total of 28 sets of experiments were completed, with each set repeated three times to eliminate chance factors, and the average value was recorded as the result for each set of experiments. The motion diagram, depicted in Figure 13 with the yellow ball serving as the motion reference, presents the annotated motion time series map to show the average velocity results of the robot, as illustrated in Figure 14. The swimming velocity of the bionic mantis shrimp robot is influenced primarily by the swing angular frequency of its pleopods. The robot achieves a maximum average velocity of 0.112 m/s when the swing angular frequency is 2.5π rad/s and the phase difference is $1/5Fre$. Although the phase difference among the five pairs of pleopods has a minimal effect on the robot's velocity, the phase difference significantly affects the stability of the robot's motion during the experiment.

5.1.2 | Straight line kinetic verification experiment

Figure 15 presents a sequence of motion images showing the bionic mantis shrimp robot in a cycle, displaying the motion state of the pleopod at different moments. When the pleopod swings backward, each joint of the pleopod reaches its mechanical limit to maximize the water contact area and provide thrust for the

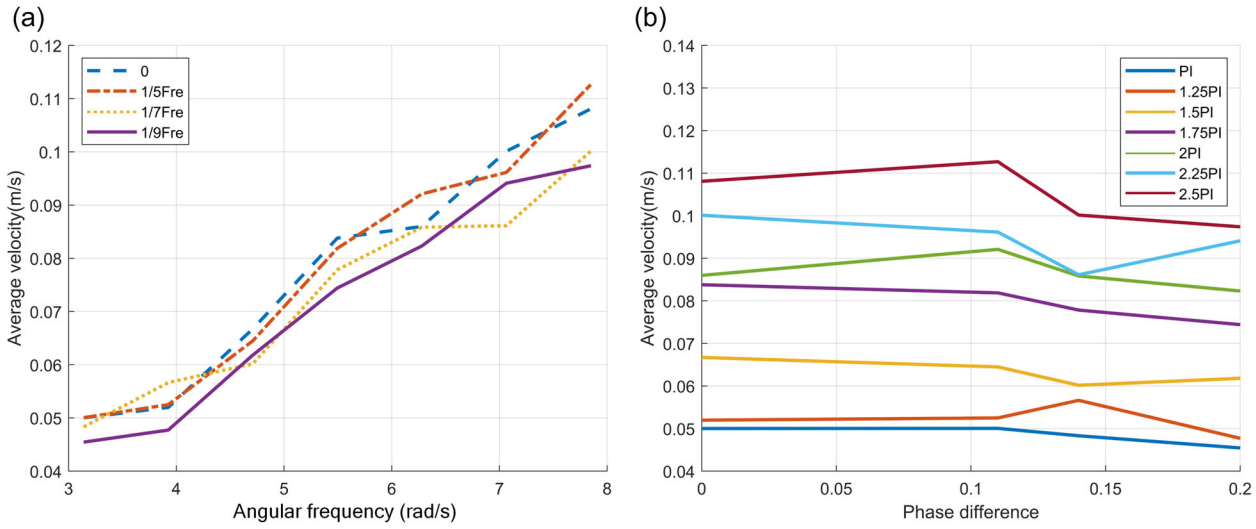

FIGURE 14 Curve showing the influence of the phase difference and angular frequency of the pleopod movement on velocity. (a) Effect of frequency on velocity. (b) Effect of phase difference on velocity. [Color figure can be viewed at wileyonlinelibrary.com]

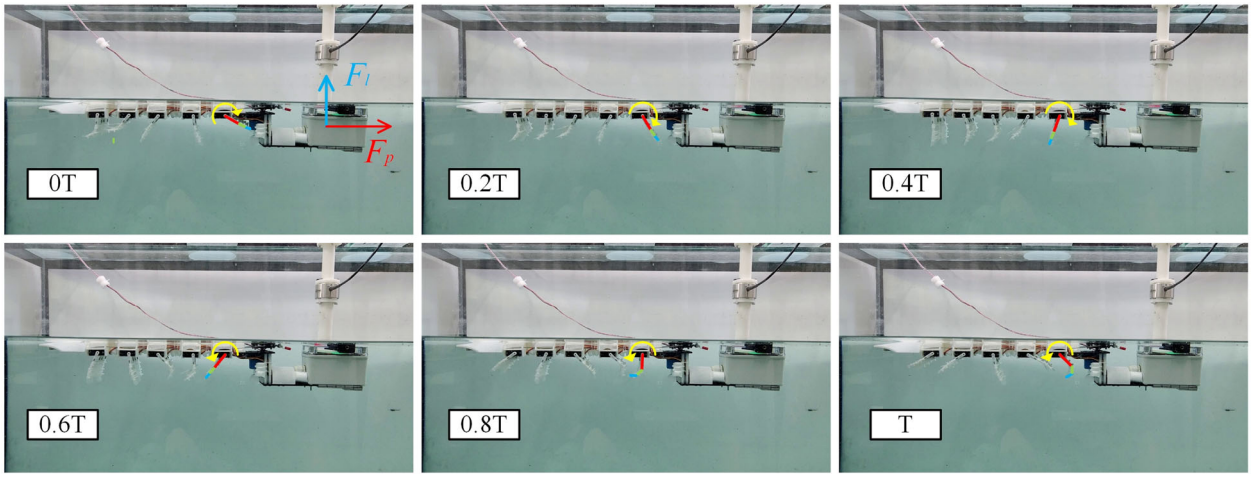

FIGURE 15 Diagram of the straight motion process of the robot with a fixed head.]

robot. Conversely, when the pleopod swings forward, the first and second joints of the pleopod bend due to water resistance. Because the robot possesses five pairs of pleopods and the motion state of each pair of pleopods varies at each moment, it is crucial to analyze the thrust at each moment for subsequent robot motion control.

In the experiment, the angular frequency of the robot's motion was set at 2.25π rad/s, and the phase difference was 1/5Fre. The changes in propulsion were measured using a six-axis force sensor installed on the upper part of the robot. Figure 16 presents a comparative analysis between the test results and the theoretical calculations. It is evident from the figure that the experimental and theoretical values of the propulsion force and lift force on the robot exhibit similar trends of change, albeit with a significant difference in amplitude. The theoretical calculations and experimental results show that the peak forward thrusts are approximately 0.93 and 0.92 N, respectively, which are nearly identical. The low points of the propulsive force are approximately −0.05 and 0.12 N for the theoretical calculation and experimental results, respectively. The maximum error in the propulsive force is 0.47 N, with an average error of 0.20 N. The maximum lift error is 0.31 N, and the average lift error is 0.12 N.

The reasons for the discrepancy in the experimental results can be attributed to the following factors: (1) due to the small effective area of the experimental tank, the movement of the robot causes fluctuations in the water surface, resulting in additional shock; (2) during the experiment, the robot's pleopod is made of resin material and a 1 mm silica gel film. The movement of the pleopod causes elastic deformation of the silica gel film, which may create a connection gap.

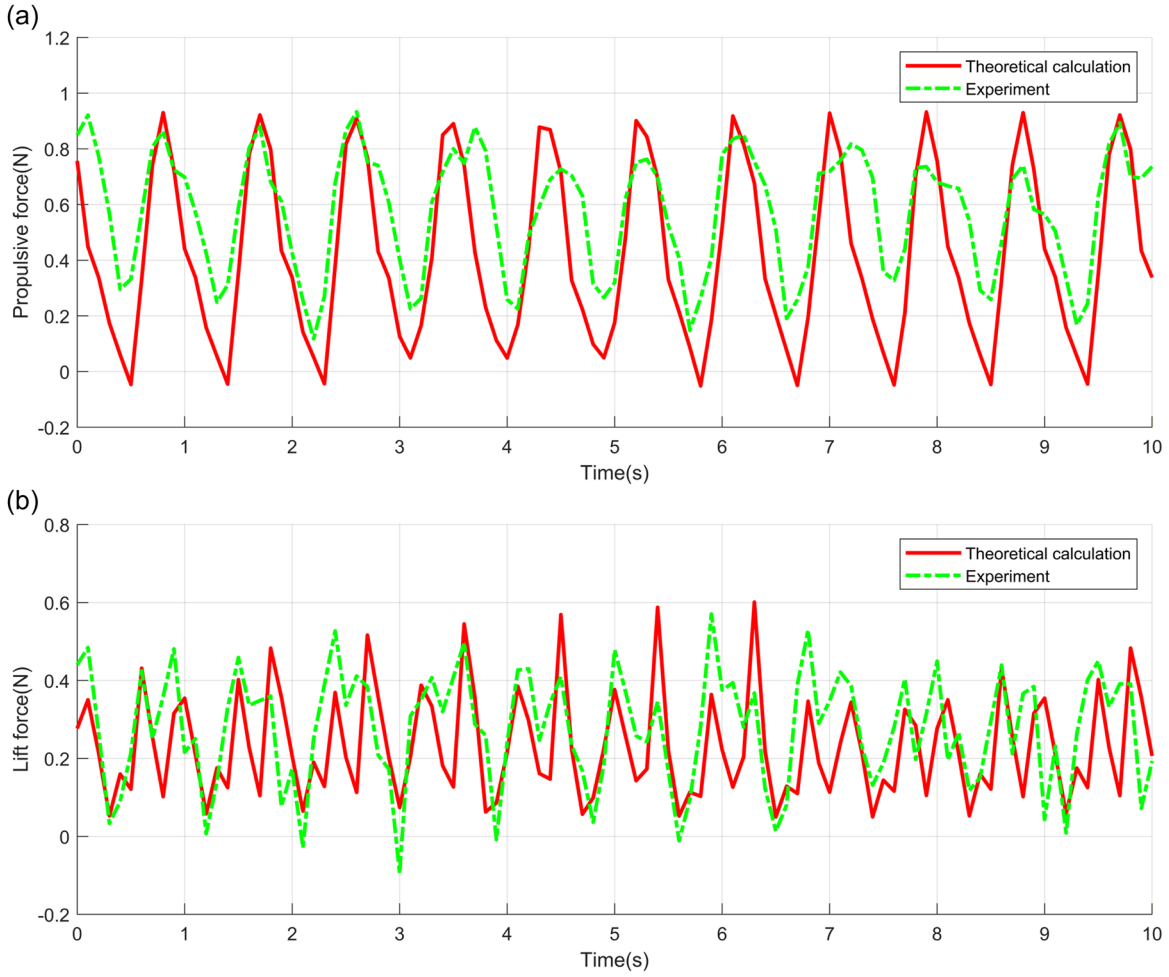

FIGURE 16 Dynamic results of the straight swimming motion of the robot with a fixed head. (a) Forward propulsion curve. (b) Forward lift curve.

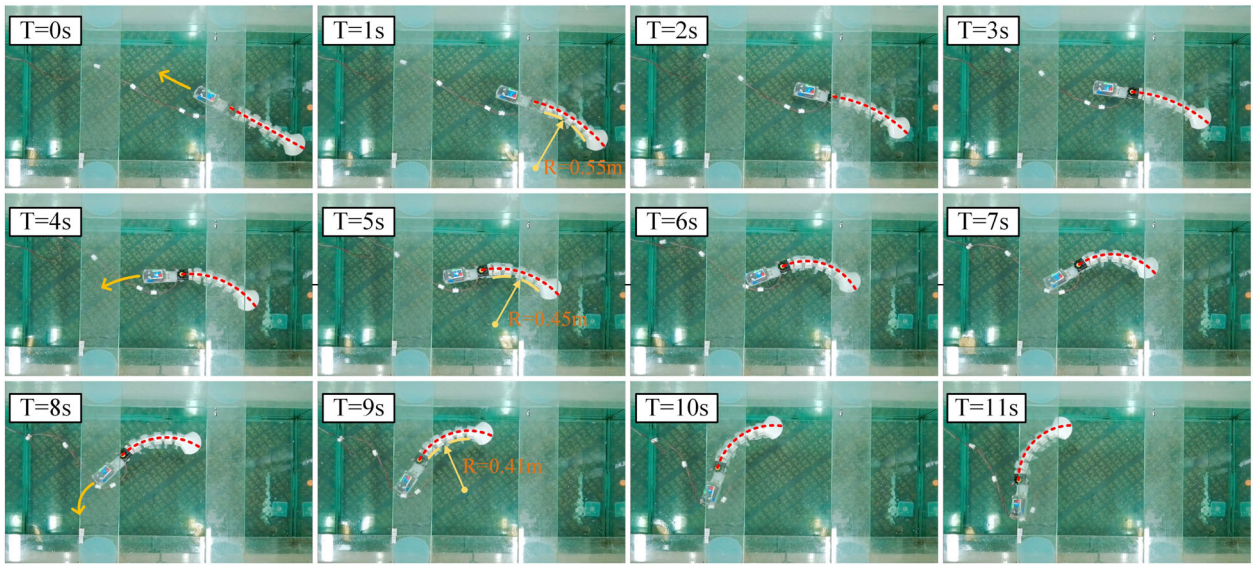

FIGURE 17 Sequence diagram of the turning motion process of the robot.]

5.2 | Turning motion experiment

5.2.1 | Robot turning motion

The turning motion of the bionic mantis shrimp robot is achieved through the bending of the flexible spine combined with the motion of the pleopod. The turning radius of the motion directly correlates with the curvature of the spine. Figure 17 depicts the turning process of the robot with a motion frequency of 3π rad/s. The bending degree of the flexible spine was adjusted to 15°, 25°, and 35° during the entire movement of the robot, resulting in corresponding turning radii of 0.55, 0.45, and 0.41 m, respectively. The overall motion of the robot was stable during the turning process, indicating good motion controllability.

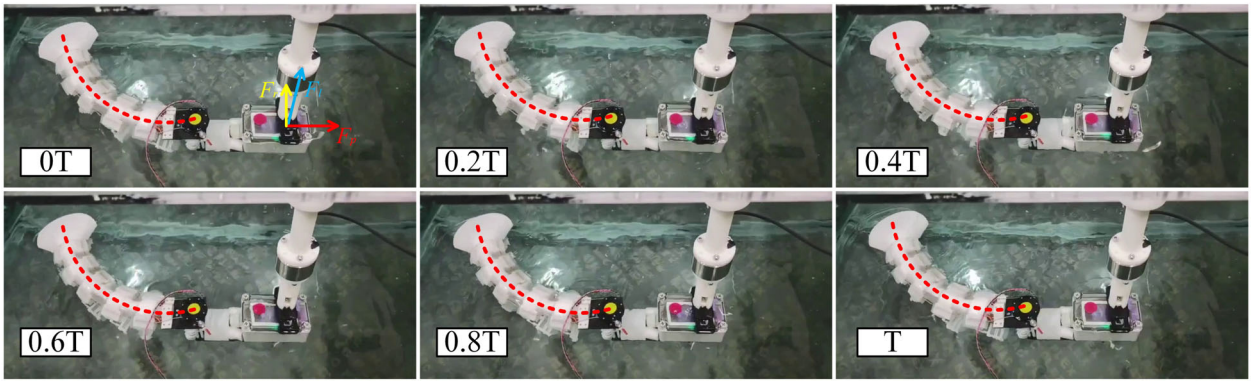

FIGURE 18 Turning motion under the fixed head of the robot.

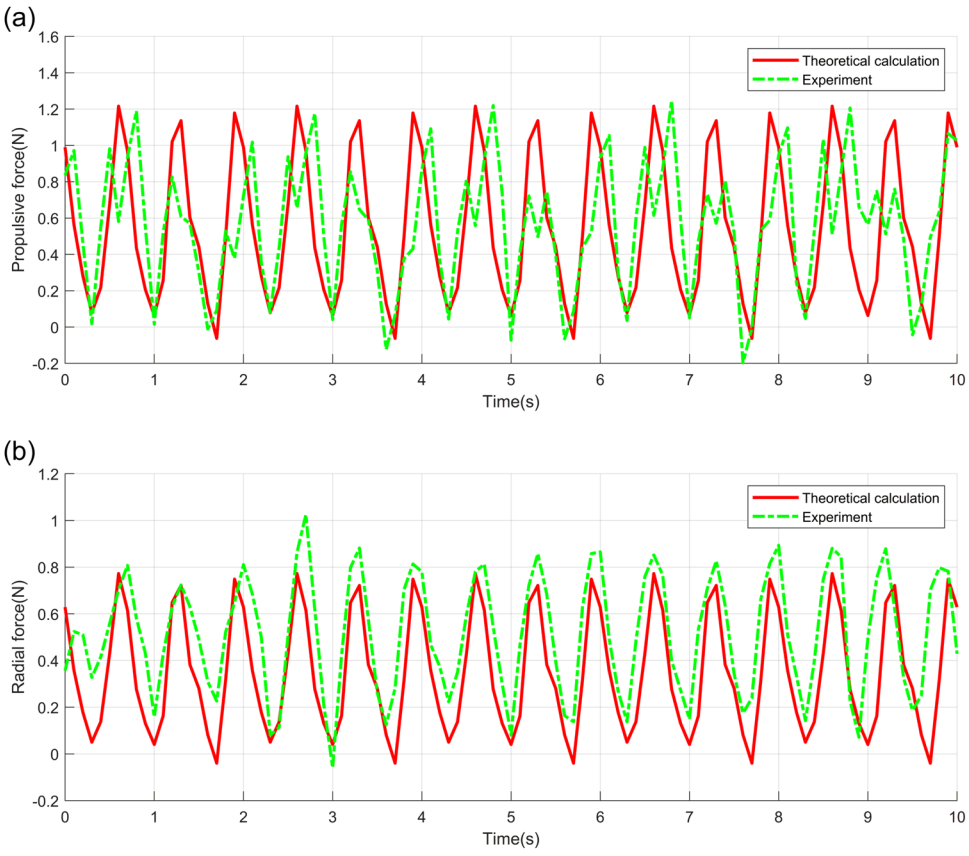

FIGURE 19 Results of the turning dynamics with the fixed head of the robot: (a) propulsion curve and (b) lift curve.

5.2.2 | Turning dynamics verification experiment

Figure 18 illustrates the sequence of periodic motion images of the robot while it is bending. The pleopod swing frequency is 3π, and the robot's bending angle is 35°.

In Figure 19, the propulsion and radial force are displayed, showing similar trends between the theoretical calculations and experimental data. In Figure 19a, the peak propulsion values for the theoretical calculation and experimental results are approximately 1.22 and 1.25 N, respectively. The low points of the theoretical calculation and experimental results are approximately −0.06 and −0.2 N, respectively. The maximum propulsive force error is 0.52 N, and the average propulsive force error is 0.29 N. The fluctuation in the propulsive force at the peak is mainly caused by water surface fluctuations and force sensor rod jitter.

The radial force, as measured in Figure 19b, represents the turning force of the robot. It exhibits a stable periodic change, verifying the smooth movement of the robot. In Figure 19b, the peak propulsion values for the theoretical calculation and experimental results are approximately 0.73 and 1.02 N, respectively. The low points of the theoretical calculation and experimental results are approximately −0.06 and −0.05 N, respectively. The maximum radial force error is 0.22 N, and the average propulsive force error is 0.16 N. The unequal length and width of the pool result in a relatively narrow water surface, which fluctuates when the robot moves, influencing its movement to a certain extent.

5.2.3 | Force analysis of the robot under different bending degrees

Figure 20 displays the turning force and lift force of the robot measured by a six-axis force sensor. The angular frequency of the robot's motion during the experiment was 3π rad/s. In Figure 20a, the different bending degrees of the robot (0°, 15°, 25°, and 35°) are presented while turning left, showing the flexibility of the flexible torso. Figure 20b depicts the measured lift force graph, indicating that the lift of the robot remains independent of the bending degree and is subject to fluctuations caused by disturbances in water flow. Figure 20c presents the measured radial force diagram, illustrating that as the bending degree of the robot's torso increases (0°, 15°, 25°, and 35°), the corresponding maximum radial forces are 0.42, 0.56, 0.71, and 0.91 N, respectively. This indicates that the robot's turning ability improves with an increase in the degree of torso bending.

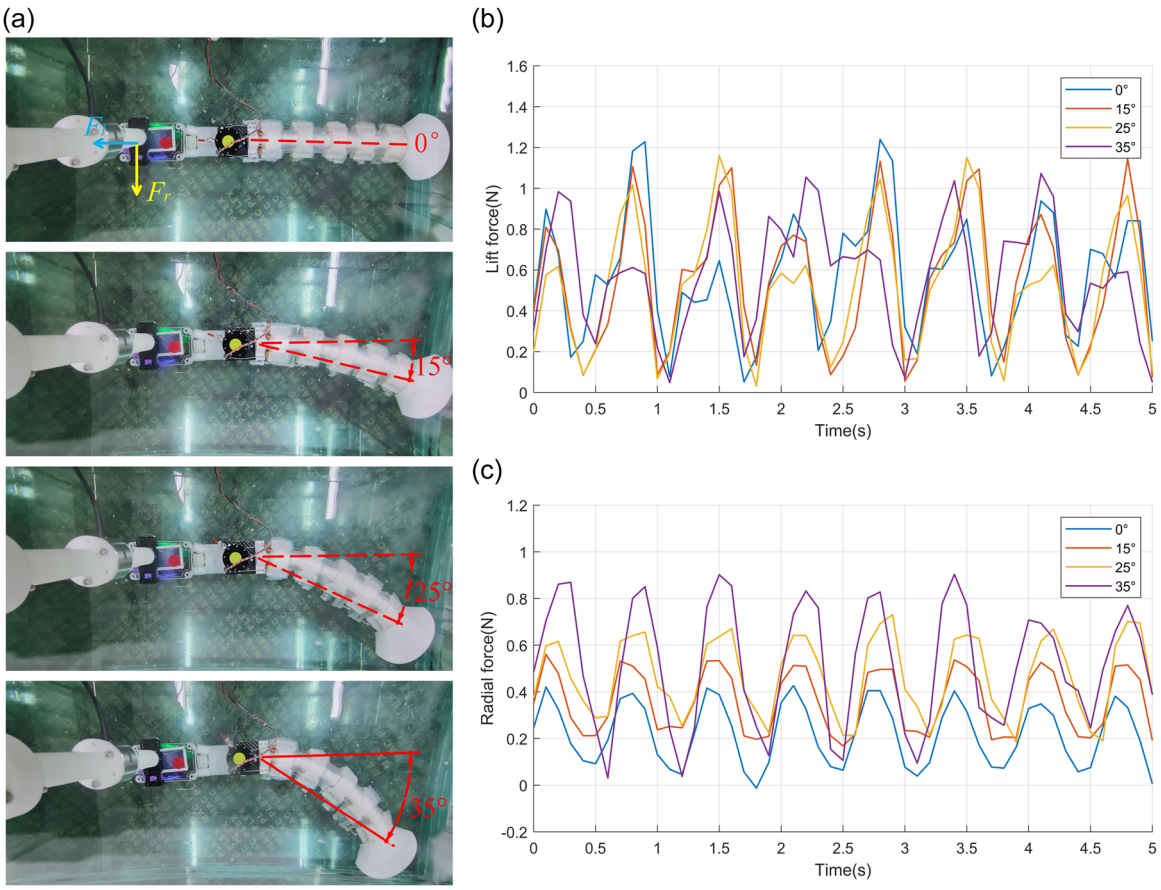

FIGURE 20 Results of robot motion under different degrees of turning. (a) Experimental process diagram of the robot under different turning amplitudes. (b) Lift curves under different turning amplitudes. (c) Turning force curves under different turning amplitudes.

6 | CONCLUSION

This paper describes the design of a bionic mantis shrimp robot system based on the physiological structure and motion characteristics of biological mantis shrimp. The force and motion laws of the robot in the world coordinate system are studied, and the torso kinematics model and swimming dynamics model of the bionic mantis shrimp robot are established and verified through experiments. In the straight swimming experiment, the robot's motion velocity is influenced mainly by the frequency of pleopod movement, and the maximum swimming velocity of the robot can reach 0.112 m/s. In the turning experiment, the robot demonstrated good motion stability and was able to complete turning motions of different radii. The experiment also revealed that the phase difference between the five pairs of pleopods greatly affects the robot's stability. Therefore, finding an efficient working interval with optimal robot velocity and stability is crucial for future research.

In future work, Fluent fluid dynamics simulations will be combined with force analysis of the bionic mantis shrimp robot in water (Adkins & Yan, 2006). The mechanism design and motion control algorithms will be optimized to improve the swimming efficiency and flexibility of the robot. Additionally, vision sensors will be incorporated to enhance the robot's ability to perceive the underwater environment and expand its potential applications in marine reconnaissance, seabed exploration, and rescue (Gašparović et al., 2023; Yan et al., 2023).

ACKNOWLEDGMENTS

This work is financially supported by National Natural Science Foundation of China (Nos. 52275037, 51875528, and 41506116), Zhejiang Provincial Natural Science Foundation of China (No. LR24E050002), the Key Research and Development Project of Zhejiang Province (No. 2023C03015), the Emergency Management Research and Development Project of Zhejiang Province (No. 2024YJ026), the Key Research and Development Project of Ningxia Hui Autonomous Region (No. 2023BDE03002), and the Fundamental Research Funds of Zhejiang Sci-Tech University (No. 24242088-Y).

REFERENCES

Adkins, D. & Yan, Y.Y. (2006) CFD simulation of fish-like body moving in viscous liquid. *Journal of Bionic Engineering*, 3, 147–153.

Am Ende, B.A. (2001) 3D mapping of underwater caves. *IEEE Computer Graphics and Applications*, 21, 14–20.

Cao, Z., Zhang, D. & Zhou, M. (2021) Direction control and adaptive path following of 3-D snake-like robot motion. *IEEE Transactions on Cybernetics*, 52, 10980–10987.

Chang, A.H. & Vela, P.A. (2020) Shape-centric modeling for control of traveling wave rectilinear locomotion on snake-like robots. *Robotics and Autonomous Systems*, 124, 103406.

Chen, G., Tu, J., Ti, X., Wang, Z. & Hu, H. (2021) Hydrodynamic model of the beaver-like bendable webbed foot and paddling characteristics under different flow velocities. *Ocean Engineering*, 234, 109179.

Chen, G., Xu, Y., Wang, Z., Tu, J., Hu, H., Chen, C. et al. (2024) Dynamic tail modeling and motion analysis of a beaver-like robot. *Nonlinear Dynamics*, 112, 6859–6875.

Chen, G., Xu, Y., Yang, C., Yang, X., Hu, H., Chai, X. et al. (2023) Design and control of a novel bionic mantis shrimp robot. *IEEE/ASME Transactions on Mechatronics*, 28, 3376–3385.

Chen, G., Xu, Y., Yang, X., Hu, H., Cheng, H., Zhu, L. et al. (2024) Target tracking control of a bionic mantis shrimp robot with closed-loop central pattern generators. *Ocean Engineering*, 297, 116963.

Chen, G., Zhao, Z., Lu, Y., Yang, C. & Hu, H. (2024) Deep reinforcement learning-based pitch attitude control of a beaver-like underwater robot. *Ocean Engineering*, 307, 118163.

Cheng, J., Zhang, Z., Li, Y., Zhang, L., Hui, M. & Sha, Z. (2024) Rolling with the punches: organism-environment interactions shape spatial pattern of adaptive differentiation in the widespread mantis shrimp *Oratosquilla oratoria*. *Science of the Total Environment*, 917, 170244.

Cong, Y., Gu, C., Zhang, T. & Gao, Y. (2021) Underwater robot sensing technology: a survey. *Fundamental Research*, 1, 337–345.

Cox, S.M., Schmidt, D., Modarres-Sadeghi, Y. & Patek, S.N. (2014) A physical model of the extreme mantis shrimp strike: kinematics and cavitation of Ninjabot. *Bioinspiration & Biomimetics*, 9, 016014.

Crespi, A., Lachat, D., Pasquier, A. & Ijspeert, A.J. (2008) Controlling swimming and crawling in a fish robot using a central pattern generator. *Autonomous Robots*, 25, 3–13.

Fu, S., Wei, F., Yin, C., Yao, L. & Wang, Y. (2021) Biomimetic soft microswimmers: from actuation mechanisms to applications. *Biomedical Microdevices*, 23, 6.

Gašparović, B., Mauša, G., Rukavina, J. & Lerga, J. (2023) Evaluating Yolov5, Yolov6, Yolov7, and Yolov8 in underwater environment: is there real improvement? In: *2023 8th International Conference on Smart and Sustainable Technologies (SpliTech), 20-23 June 2023, Split/Bol, Croatia*. IEEE. pp. 1–4.

Huang, J., Gong, X., Wang, Z., Xue, X., Yang, X., Liang, J., et al. (2016) The kinematics analysis of webbed feet during cormorants' swimming. In: *2016 IEEE International Conference on Robotics and Biomimetics (ROBIO), 03-07 December 2016, Qingdao, China*. IEEE. pp. 301–306.

Ito, F., Ishii, Y., Kurumaya, S., Kagaya, K. & Nakamura, T. (2024) A design method for instantaneous force generation based on a mantis shrimp with exoskeleton spring. *IEEE/ASME Transactions on Mechatronics*, 29, 960–971.

Kashem, S. & Sufyan, H. (2017) A novel design of an aquatic walking robot having webbed feet. *International Journal of Automation and Computing*, 14, 576–588.

Li, Z., Du, R., Lei, M.C. & Yuan, S.M. (2011) Design and analysis of a biomimetic wire-driven robot arm. In: *ASME International Mechanical Engineering Congress and Exposition*. Denver, Colorado, USA: ASME. pp. 191–198.

Ni, J., Chen, Y., Tang, G., Shi, J., Cao, W. & Shi, P. (2023) Deep learning-based scene understanding for autonomous robots: a survey. *Intelligence & Robotics*, 3, 374–401.

Patek, S. (2015) The most powerful movements in biology. *American Scientist*, 103, 330–338.

Pendergast, D.R. & Lundgren, C.E.G. (2009) The underwater environment: cardiopulmonary, thermal, and energetic demands. *Journal of Applied Physiology*, 106, 276–283.

Reddy, P., Pradeepa, M., Venkatakiran, S., Walia, R. & Saravanan, M. (2021) Image and signal processing in the underwater environment. *Journal of Nuclear Energy Science & Power Generation Technology*, 10, 2.

Ren, K. & Yu, J. (2021) Research status of bionic amphibious robots: a review. *Ocean Engineering*, 227, 108862.

Scaradozzi, D., Palmieri, G., Costa, D. & Pinelli, A. (2017) BCF swimming locomotion for autonomous underwater robots: a review and a novel solution to improve control and efficiency. *Ocean Engineering*, 130, 437–453.

Streets, A., England, H. & Marshall, J. (2022) Colour vision in stomatopod crustaceans: more questions than answers. *Journal of Experimental Biology*, 225, jeb243699.

Tadayon, M., Amini, S., Masic, A. & Miserez, A. (2015) The mantis shrimp saddle: a biological spring combining stiffness and flexibility. *Advanced Functional Materials*, 25, 6437–6447.

Thoen, H.H., How, M.J., Chiou, T.H. & Marshall, J. (2014) A different form of color vision in mantis shrimp. *Science*, 343, 411–413.

Wang, R., Zhang, C., Zhang, Y., Tan, W., Chen, W. & Liu, L. (2023) Soft underwater swimming robots based on artificial muscle. *Advanced Materials Technologies*, 8, 2200962.

Wang, X., Zhao, J., Pei, X., Wang, T., Hou, T. & Yang, X. (2024) Bioinspiration review of Aquatic Unmanned Aerial Vehicle (AquaUAV). *Biomimetic Intelligence and Robotics*, 4, 100154.

Weidner, N., Rahman, S., Li, A.Q. & Rekleitis, I. (2017) Underwater cave mapping using stereo vision. In: *2017 IEEE International Conference on Robotics and Automation (ICRA)*, 29 May 2017 - 03 June 2017, Singapore. IEEE. pp. 5709–5715.

Xu, M., Cao, Y., Sun, X., Miao, Y., Dong, X., Zhang, Y. et al. (2022) Circular polarization detection metasurface inspired by the polarized vision of mantis shrimp. *Optics Communications*, 507, 127599.

Yan, T., Xu, Z., Yang, S.X. & Gadsden, S.A. (2023) Formation control of multiple autonomous underwater vehicles: a review. *Intelligence & Robotics*, 3, 1–22.

Yang, Z., Gong, W., Chen, H., Wang, S. & Zhang, G. (2022) Research on the turning maneuverability of a bionic robotic dolphin. *IEEE Access*, 10, 7368–7383.

Yu, J., Wang, M., Dong, H., Zhang, Y. & Wu, Z. (2018) Motion control and motion coordination of bionic robotic fish: a review. *Journal of Bionic Engineering*, 15, 579–598.

Zhang, Z., Yang, G. & Yeo, S.H. (2011) Inverse kinematics of modular cable-driven snake-like robots with flexible backbones. In: *2011 IEEE 5th International Conference on Robotics, Automation and Mechatronics (RAM), 17-19 September 2011, Qingdao, China*. IEEE. pp. 41–46.